Supplementary Information to:

Directional freeze-cast hybrid-backbone meso-macroporous bodies as micromonolith catalysts for gas-to-liquid processes

Jonglack Kim,[a, ‡] Valentina Nese,[a, ‡] Jochen Joos,[b] Kai Jeske,[a] Nicolas Duyckaerts,[a] Norbert Pfänder,[c] and Gonzalo Prieto[a,*]

[a] Max-Planck-Institut für Kohlenforschung, Kaiser-Wilhelm-Platz 1, 45470 Mülheim an der Ruhr (Germany)

[b] Institute for Applied Materials (IAM-WET), Karlsruhe Institute of Technology (KIT), Adenauerring 20b, 76131, Karlsruhe (Germany)

[c] Max-Planck-Institut für Chemische Energiekonversion, Stiftstraße 34-36, 45470 Mülheim an der Ruhr (Germany)

‡: These authors contributed equally to this work.

* Email: prieto@mpi-muelheim.mpg.de

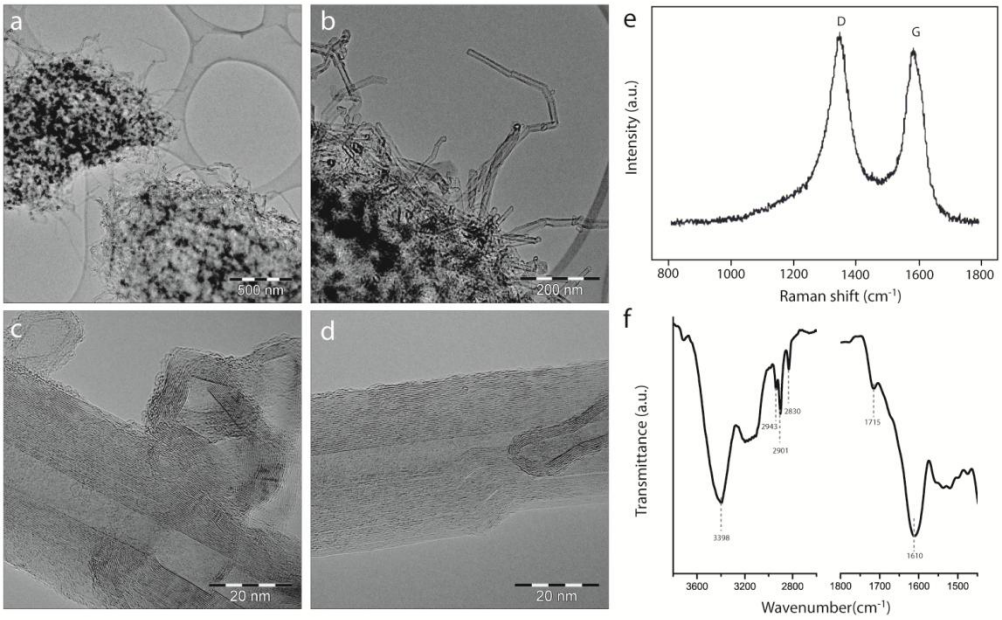

Figure S1: Physicochemical characterization of multiwall carbon nanotubes. a, b) Overview bright-field TEM micrographs. c,d) high-resolution bright-field TEM micrographs. e) Raman spectra. f) Fourier-Transform Infrared spectra.

(HR)TEM inspection of the carbon nanotubes clearly reveals their multiwall nature and highly developed graphitic structure. The tubes display diameters in the range of 10-40 nm and lengths of about 10-30 μm, which are ideal to achieve a highly interlaced network as the scaffold for the monolith backbone. The Raman spectra shows well developed so-called D and G bands peaking at Raman-shifts of ca. 1345 and 1575 cm^{-1}, respectively, indicative for the presence of local defects and a certain degree of structural disorder in the tubes. The FTIR spectra showed bands at 2830, 2901 and 2943 cm^{-1}, corresponding to the stretching vibrations in alkyl CH_x species, likely associated to partially hydrogenated defects on the surface of the CNTs. In addition, a broad band in the region 2500-3000 cm^{-1}, alongside a signal at 1715 cm^{-1} can be ascribed to stretching vibrations of -OH and C=O groups in carboxylic species, confirming the surface functionalization of the nanotubes with carboxylic groups, which facilitates their suspension in the aqueous medium employed to cast the monoliths.

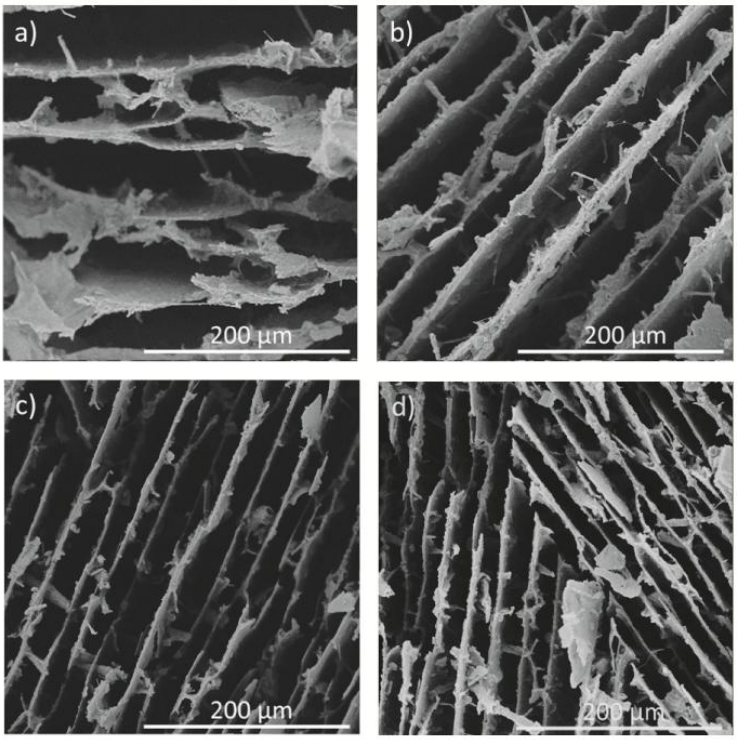

Figure S2: Representative cross-sectional SEM micrographs for CNT-Al_2O_3 monoliths cast in the absence of zirconium acetate as ice growth modulator at cooling rates of a) -0.5, b) -2.0, c) -5.0 and d) -10 K min^{-1}.

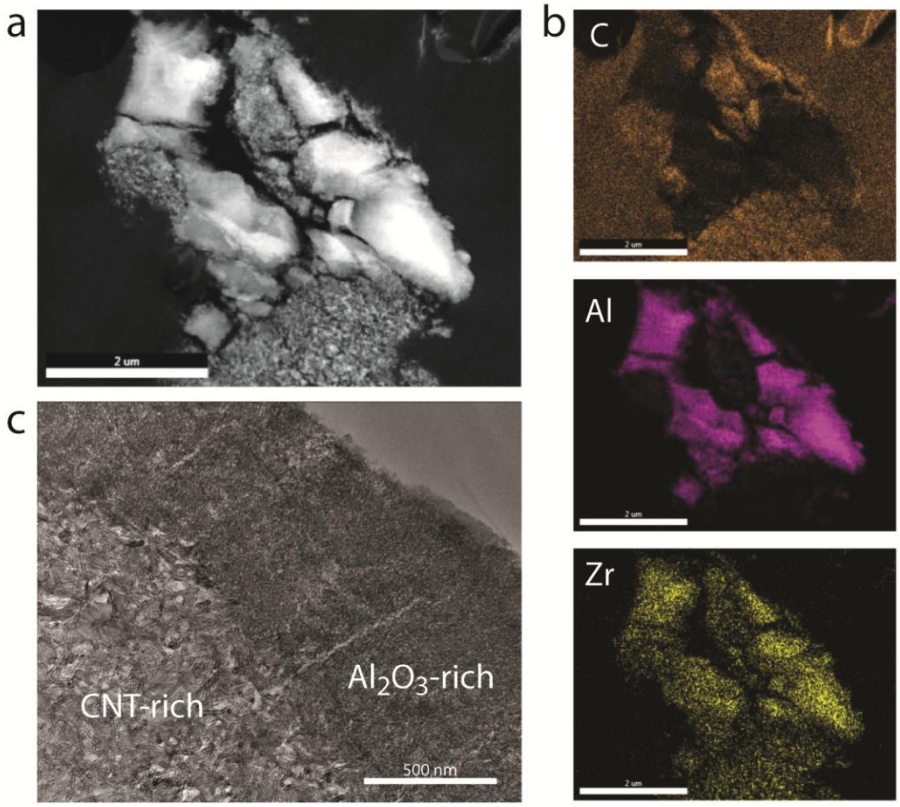

Figure S3: a) Representative HAADF-STEM micrograph of an ultramicrotomed cross-section (150 nm nominal thickness) of a CNT-$ZrAlO_x$ micromonolith freeze-cast from a suspension obtained by thorough wet milling of the CNT and pseudoboehmite solid precursors in water. b) EDX compositional maps of the region in panel (a) obtained from the corresponding K-spectral lines. c) Bright-field TEM micrograph showing a high magnification detail of CNT and Al_2O_3-rich patches, as labelled on the micrograph. Scale bars are 2 μm for panels a and b. Scale bar is 500 nm for panel c.

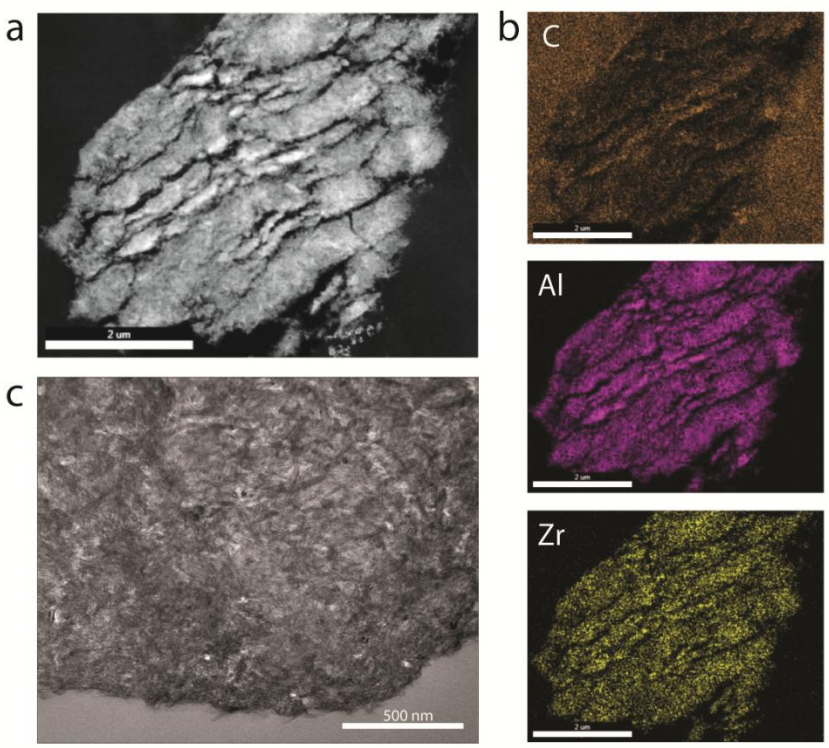

Figure S4: a) Representative HAADF-STEM micrograph of an ultramicrotomed cross-section (150 nm nominal thickness) of a CNT-$ZrAlO_x$ micromonolith freeze-cast from a suspension obtained by high-power ultrasonication of the CNT and pseudoboehmite solid precursors in water using a cell disruptor homogenizer. b) EDX compositional maps of the region in panel (a) obtained from the corresponding K-spectral lines. c) Bright-field TEM micrograph showing a high magnification detail of the excellent spatial intermixing between the CNT and $ZrAlO_x$ backbone components. Scale bars 2 μm for panels a and b. Scale bars 500 nm for panel c.

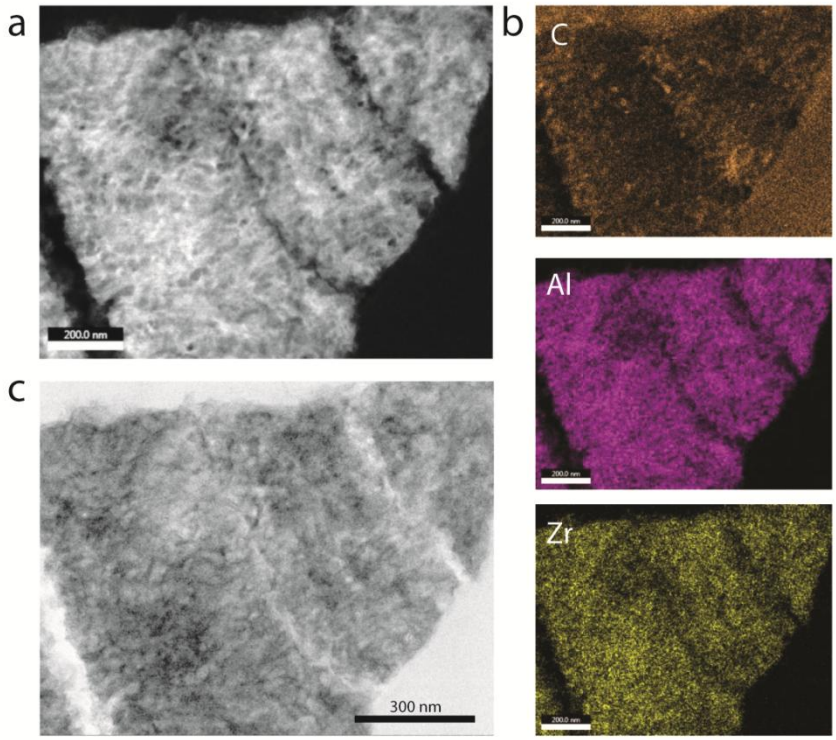

Figure S5: a) Representative HAADF-STEM micrograph of an ultramicrotomed cross-section (150 nm nominal thickness) of a CNT-$ZrAlO_x$ micromonolith freeze-cast from a suspension obtained by high-power ultrasonication of the CNT and pseudoboehmite solid precursors in water using a cell disruptor homogeneizer. b) EDX compositional maps of the region in panel (a) obtained from the corresponding K-spectral lines. c) Bright-field STEM micrograph showing a high magnification detail of the excellent spatial intermixing between the CNT and $ZrAlO_x$ backbone components. Scale bars 200 nm for panels a and b. Scale bars 300 nm for panel c.

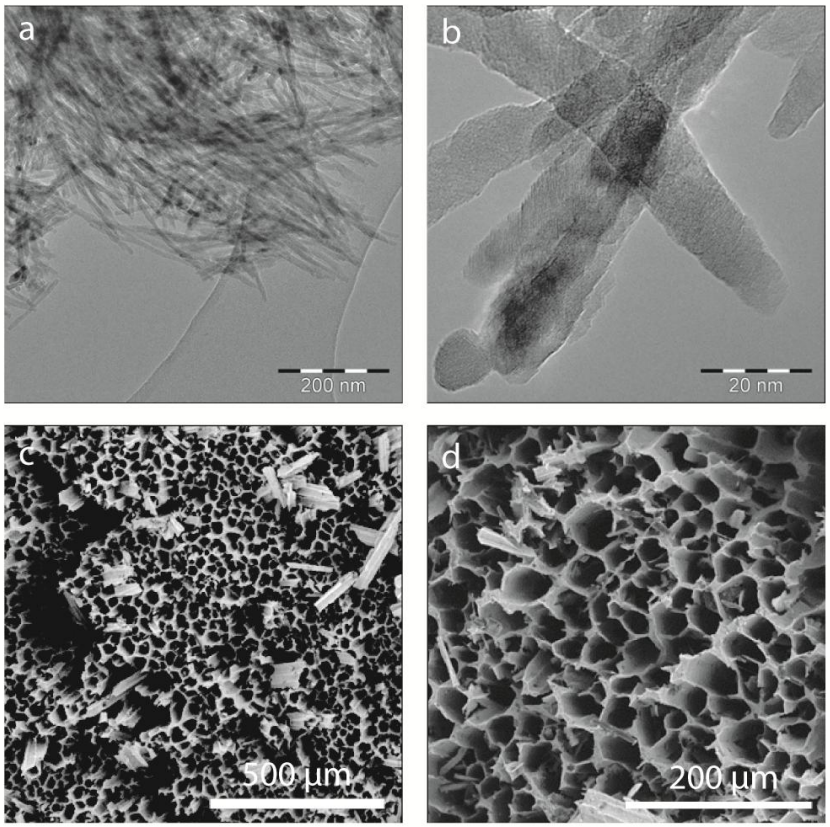

Figure S6: a,b) Representative bright-field TEM micrographs of Al_2O_3 nanofibers. c,d) Cross-sectional SEM micrographs of a ZrO_x-Al_2O_3 (MN_ZrAlO) micromonolith freeze-cast employing Al_2O_3 nanofibers as 1D skeleton component.

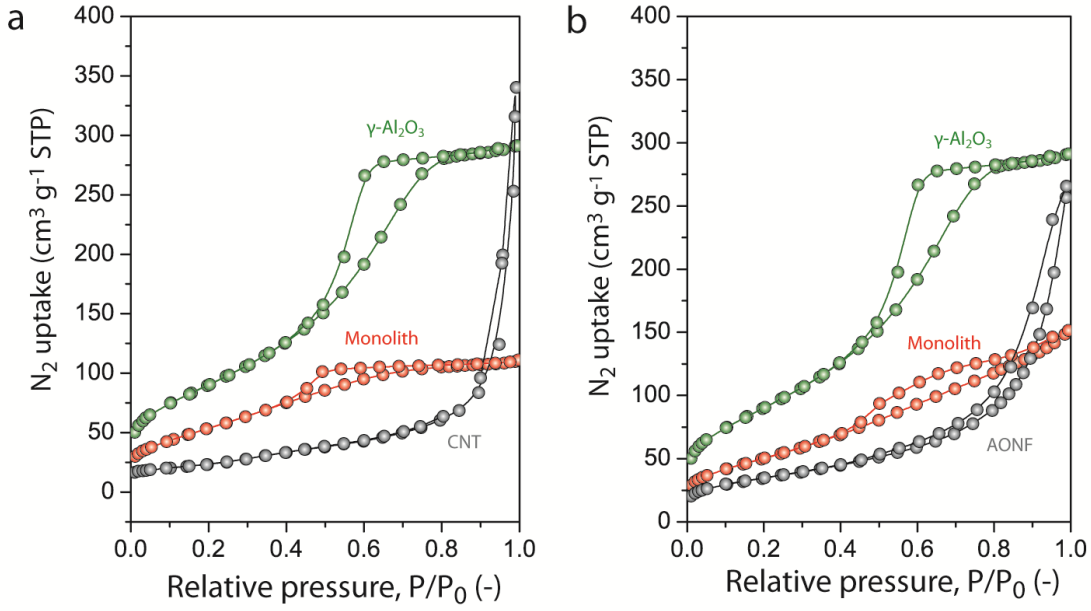

Figure S7: N_2-physisorption isotherms, recorded at 77K, for the individual building units and the freeze-cast micromonoliths with a) a CNT-$ZrAlO_x$ backbone and b) a $ZrAlO_x$ backbone. CNT: carbon nanotubes. AONF: Alumina nanofibers.

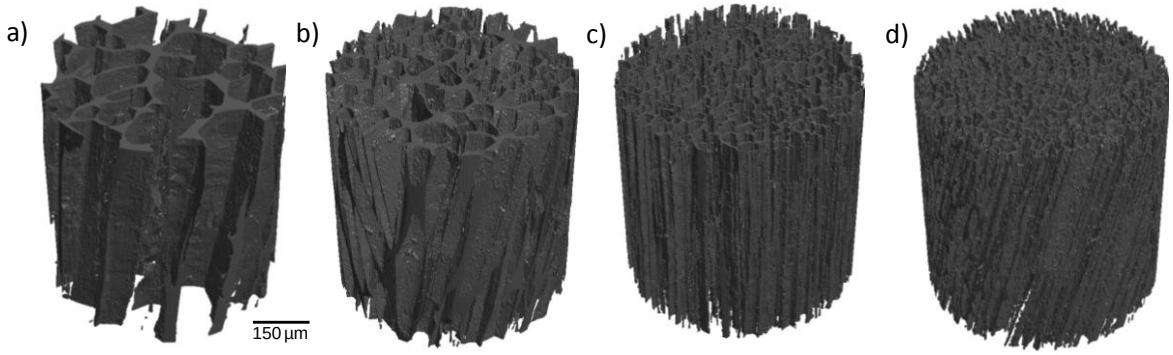

Figure S8: Representative 3D-rendered visualizations of reconstructed and segmented X-ray tomograms for CNT-$ZrAlO_x$ micromonoliths casted using cooling rates of a) -0.5, b) -2, c) -5 and d) -10 K min^{-1}, respectively, obtained at a spatial resolution corresponding to a voxel size of 850 x 850 x 850 nm^3.

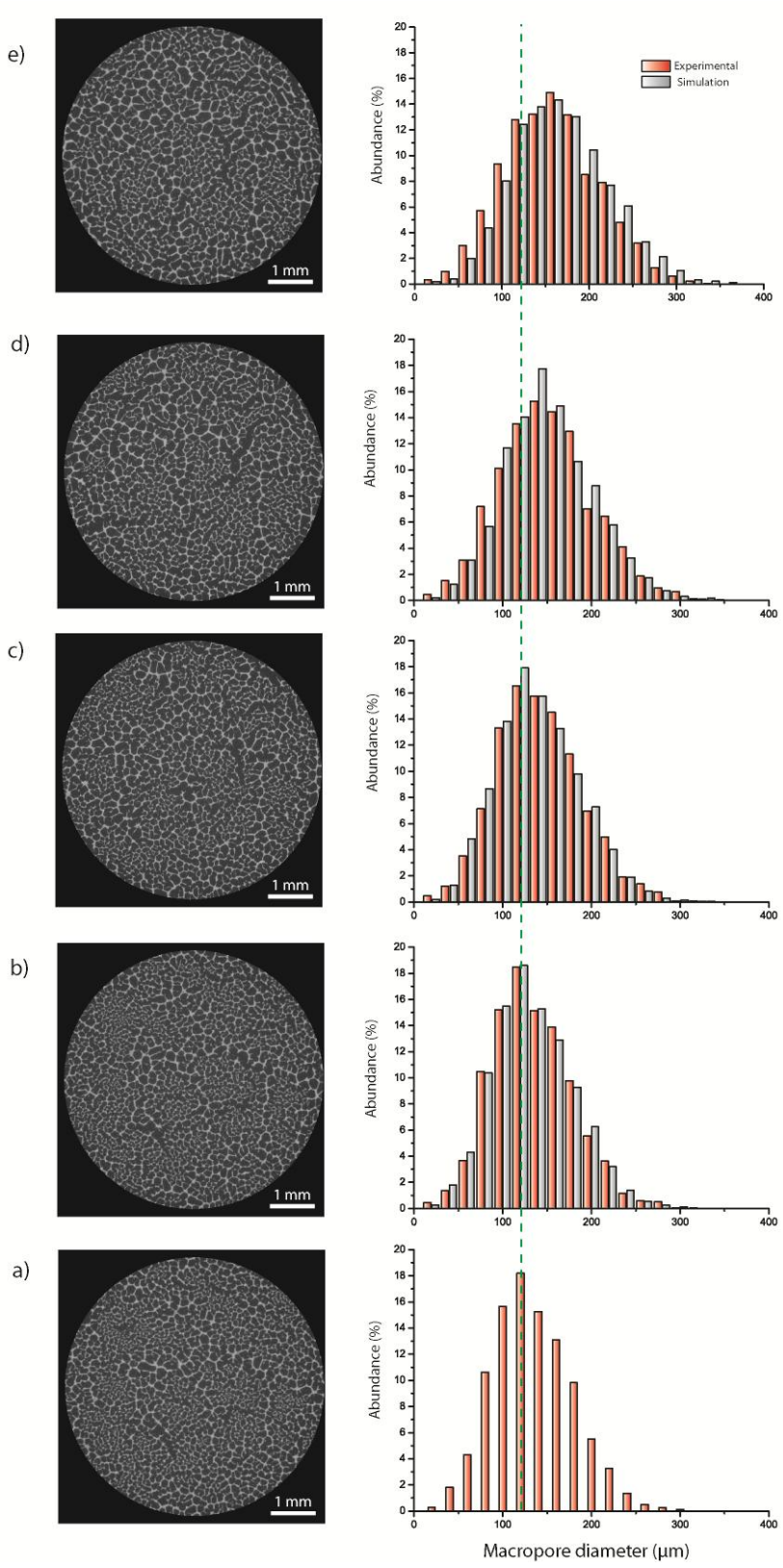

Figure S9: Cross-sectional X-ray tomography slices (left panels) and number-weighed macropore size distributions (right panels) registered at equidistant (600 µm distance between consecutive slices, from bottom (panel a) to top (panel e)) positions along the axial direction of a CNT-$ZrAlO_x$ micromonolith cast at a cooling rate of -0.5 K min^{-1}, with the corresponding number-weighed macropore size distribution as derived experimentally from the reconstructed tomograms (orange bars) and predicted by a sintering simulation of ice crystal growth (gray bars) with optimal fitting parameters (see main text). The dashed line serves as guide to the eyes to visualize the right-shift observed in the macropore size distribution while moving upwards along the axial axis of the monolith body.

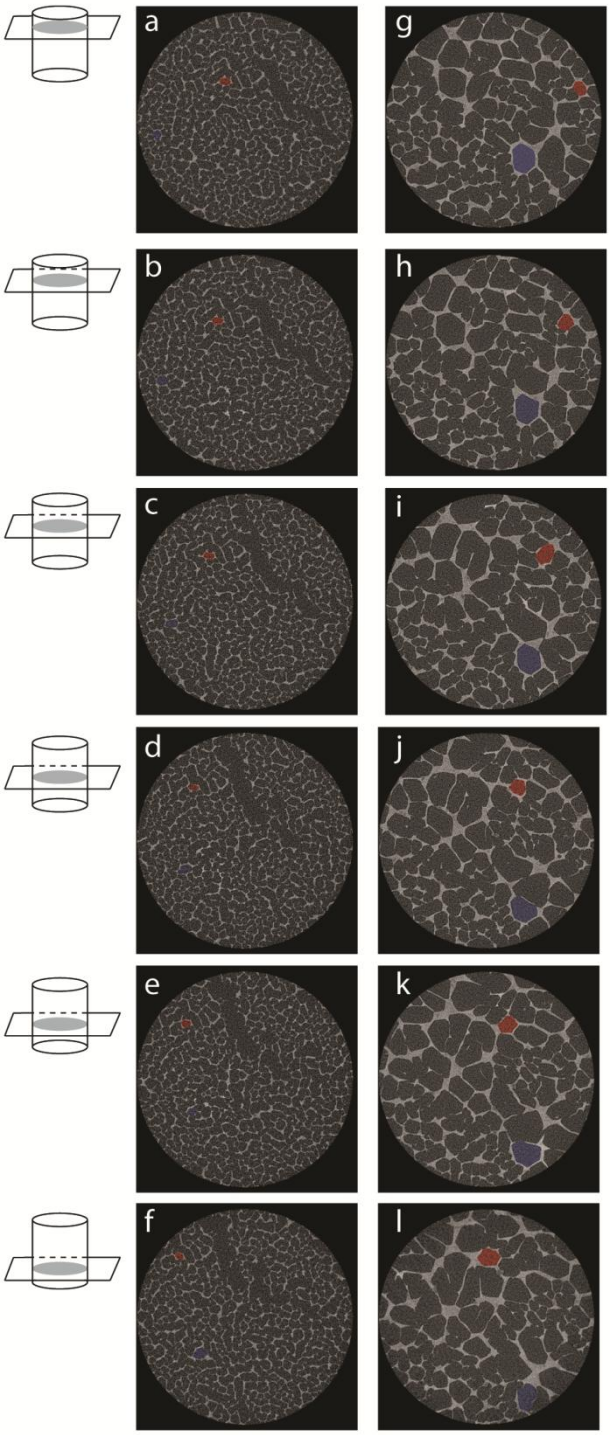

Figure S10: Labeled tracking of two selected macropores channels along axially-stacked X-ray tomographic slices for CNT/$ZrAlO_x$ micromonoliths freeze-cast with cooling rates of a-f) -10 K min^{-1} and g-l) -2 K min^{-1}.

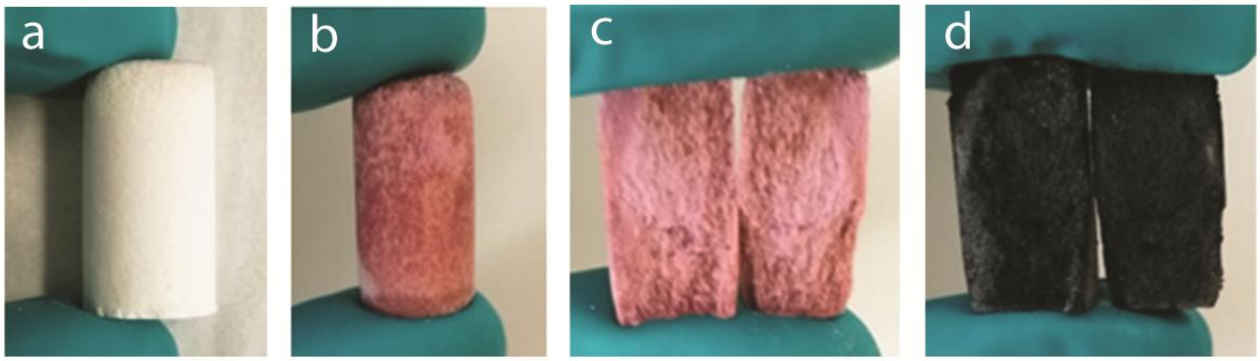

Figure S11: Photographs of a micromonolith body with a $ZrAlO_x$ backbone, a) after freeze casting, freeze drying and annealing; b) after impregnation with an aqueous solution of Ru and Co nitrate precursors and drying; c) cross-sectional view after axial slicing the monolith in panel (b); after calcination for metal nitrate decomposition into oxide nanocrystals to obtain the ultimate Fischer-Tropsch catalyst (also shown after axial sectioning).

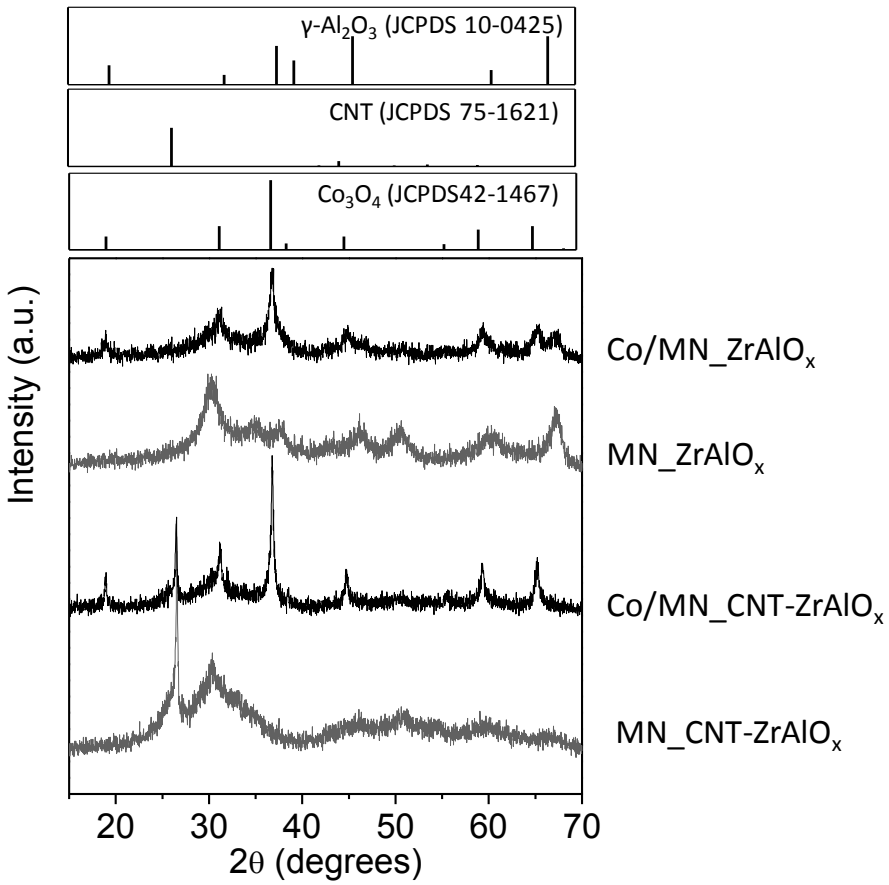

Figure S12: Powder-X-ray diffraction patterns for monolithic bodies with different backbone compositions (gray traces) and the corresponding cobalt-based Fischer-Tropsch catalysts in their as-calcined state (black traces). Reference patterns for selected crystalline phases identified in the samples are given on the top part of the plot.

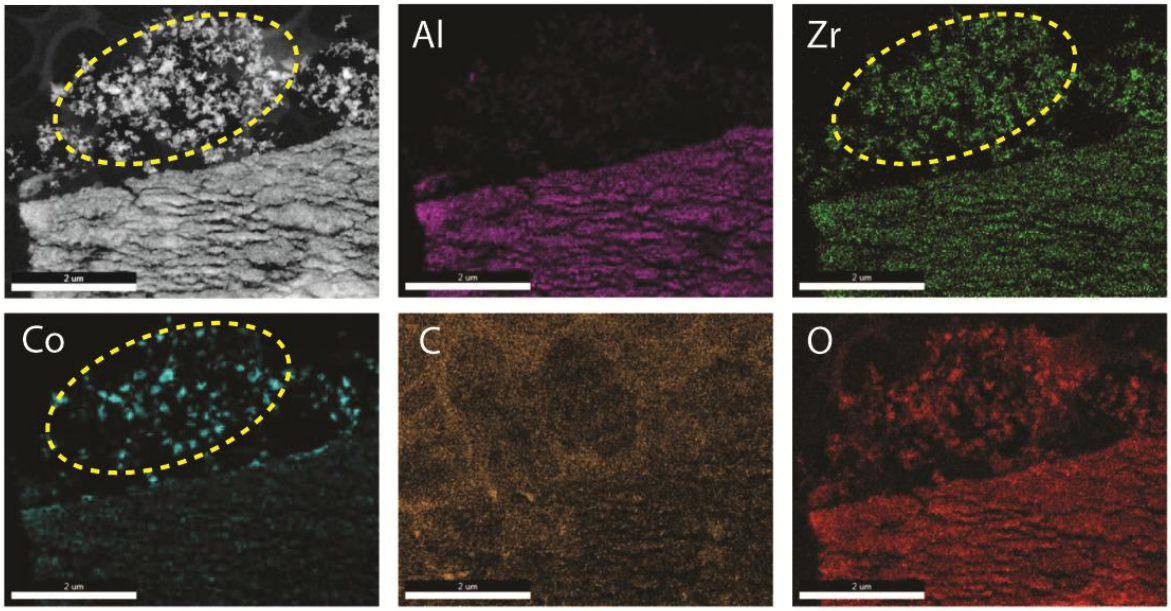

Figure S13: Representative HAADF-STEM micrograph (top-left panel) of an ultramicrotomed cross-section (150 nm nominal thickness) of a Co/CNT-ZrAlO_x micromonolithic catalyst and EDX compositional maps of the same region obtained from the corresponding K-spectral lines.

The dashed region on the micrograph and the Co, Zr-compositional maps highlights the presence of Co_3O_4 nanocrystals not directly confined to the mesoporous Al_2O_3 component of the monolith backbone, but associated to ZrO_x species which protrude from the Al_2O_3-containing monolith macropore wall and are thus not associated to Al_2O_3 nanocrystals. These ZrO_x patches might originate from Zr acetate species which remain "trapped" within the ice crystals during freeze casting, aggregate upon template removal by freeze drying and subsequent annealing treatments.